ACS APPLIED MATERIALS & INTERFACES

Research Article

Cite This: ACS Appl. Mater. Interfaces XXXX, XXX, XXX−XXX

www.acsami.org

Bi_2WO_6 Semiconductor Nanoplates for Tumor Radiosensitization through High-*Z* Effects and Radiocatalysis

Yuan Zang,[†,‡,∥] Linji Gong,[‡,§,∥] Linqiang Mei,[†,‡] Zhanjun Gu,*[,‡,§] and Qing Wang*[,†]

[†]College of Civil Engineering and Architecture, Shandong University of Science and Technology, Qingdao 266590, China

[‡]CAS Key Laboratory for Biomedical Effects of Nanomaterials and Nanosafety, Institute of High Energy Physics, Chinese Academy of Sciences, Beijing 100049, China

[§]University of Chinese Academy of Science, Beijing 100049, China

Supporting Information

ABSTRACT: The radioresistance of tumor cells is considered to be an Achilles' heel of cancer radiotherapy. Thus, an effective and biosafe radiosensitizer is highly desired but hitherto remains a big challenge. With the rapid progress of nanomedicine, multifunctional inorganic nanoradiosensitizers offer a new route to overcome the radioresistance and enhance the efficacy of radiotherapy. Herein, poly(vinylpyrrolidone) (PVP)-modified Bi_2WO_6 nanoplates with good biocompatibility were synthesized through a simple hydrothermal process and applied as a radiosensitizer for the enhancement of radiotherapy for the first time. On the one hand, the high-*Z* elements Bi ($Z = 83$) and W ($Z = 74$) endow PVP−Bi_2WO_6 with better X-ray energy deposition performance and thus enhance radiation-induced DNA damages. On the other hand, Bi_2WO_6 semiconductors exhibit significant photocurrent and photocatalytic-like radiocatalytic activity under X-ray irradiation, giving rise to the effective separation of electron/hole (e^-/h^+) pairs and subsequently promoting the generation of cytotoxic reactive oxygen species, especially hydroxyl radicals ($^•OH$). The γ-H2AX and clonogenic assays demonstrated that PVP−Bi_2WO_6 could efficiently increase cellular DNA damages and colony formations under X-ray irradiation. These versatile features endowed PVP−Bi_2WO_6 nanoplates with enhanced radiotherapy efficacy in animal models. In addition, Bi_2WO_6 nanoplates can also serve as good X-ray computed tomography imaging contrast agents. Our findings provide an alternative nanotechnology strategy for tumor radiosensitization through simultaneous radiation energy deposition and radiocatalysis.

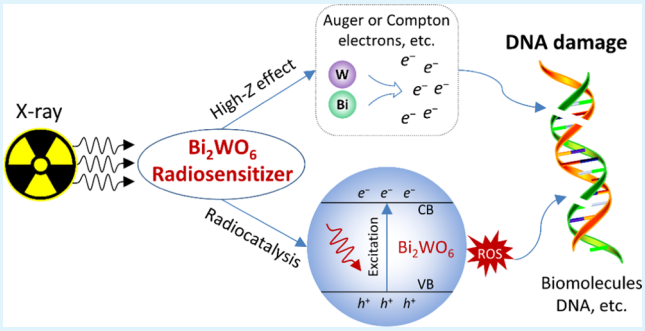

KEYWORDS: *Bi_2WO_6, radiocatalysis, radiosensitization, radiotherapy, nanomedicine*

1. INTRODUCTION

Radiotherapy, one of the most common but effective clinical anticancer therapies, kills tumor cells via focused high-energy radiation.[1] During radiotherapy, on the one hand, ionizing radiation can directly damage cellular DNA and also induce DNA damages indirectly through reactive oxygen species (ROS), which is mainly generated from the radiolysis of H_2O molecules.[2,3] However, the clinical efficacy of radiotherapy is often weakened by some limitations, such as the high doses of radiation, the side effects to normal tissues, and particularly the radioresistance. Among them, the radioresistance of tumor cells is considered to be a bottleneck of cancer radiotherapy in the clinic. Therefore, an effective and biosafe radiosensitizer to overcome the radioresistance and enhance the efficacy of radiotherapy is highly desired.[3]

With the development of nanomedicine in the past decade, multifunctional inorganic high-*Z* nanomaterials have attracted much attention and offered a new route to enhance cancer radiotherapy.[2−7] Since the relationship between the X-ray absorption coefficient (μ) and the atomic number (Z) can be expressed as $\mu = \rho Z^4/(AE^3)$, where A is the atomic mass and E is the X-ray energy,[8,9] materials that contain higher density (ρ) or possess heavy elements are inclined to have stronger X-ray attenuation ability and better X-ray absorption.[8] The strong relationship ($\mu \sim Z^4$) between the X-ray absorption coefficient and atomic number is of great significance for biomedical applications,[8] such as the development of X-ray-computed tomography (CT) contrast agents and radiosensitizers. Therefore, there is considerable interest in using high-*Z* nanomaterials as radiosensitizers to promote the deposition of X-ray energy and the emission of secondary electrons (e.g., photoelectrons, Auger electrons, Compton electrons, etc.) via photoelectric and Compton effects.[10−12] As a result, these generated low-energy and short-range electrons not only can directly act on cellular biomolecules but also can be absorbed by the surrounding H_2O molecules to promote the ROS

Received: February 27, 2019
Accepted: May 6, 2019
Published: May 6, 2019

DOI: 10.1021/acsami.9b03636
ACS Appl. Mater. Interfaces XXXX, XXX, XXX−XXX

generation, collectively inducing cell damages inside the tumors.

Among the high-Z nanomaterials, noble metals and semiconductors are the two dominant kinds of metal-based radiosensitizers used for radiotherapy.[5] For example, metallic gold nanoparticles have been theoretically and experimentally demonstrated to be a promising candidate as radiosensitizers on the basis of their easy preparation, good chemical stability, low cytotoxicity, and especially strong photoelectric absorption coefficient.[13−15] Furthermore, high-Z semiconductor nanomaterials with versatile physicochemical properties have also become the hotspot of radiosensitizers in recent years. For example, Bi-based[16−21] and W-based[22,23] semiconductor nanoparticles have been extensively explored as radiosensitizers for radiotherapy. However, those works focus only on high-Z effects and hardly elucidate the radiosensitization mechanisms from the aspect of radiocatalysis.

The mechanism of radiocatalysis is generally considered to be similar to heterogeneous photocatalysis.[24−27] Under the irradiation of high-energy X-ray, the electron (e^-) into the conduction band of semiconductor nanomaterials can be ejected after the photoelectric absorption of the incident photons, ultimately leaving behind a hole (h^+) in the valence band.[24] Then, the X-ray-triggered radiocatalytic action will induce a series of chemical and biological events. The generated lower-energy conduction band electrons may interact with molecular oxygen (O_2) to generate superoxide radicals ($^{\bullet}O_2^-$). In addition, formed valence bands h^+ are short lived, which can react with the surface-absorbed H_2O molecules to enhance the production of hydroxyl radicals ($^{\bullet}OH$). As a consequence, the generated $^{\bullet}OH$ and $^{\bullet}O_2^-$ will subsequently damage DNA or biomolecules, realizing cancer cell killing. Moreover, compared with ultraviolet photocatalysis, X-ray-induced radiocatalysis obviously has no limitation in penetration depth in biotissues and certainly boosts the impact of X-ray on tumor tissues.

In recent years, Bi_2WO_6, one of the simplest Aurivillius oxides, has been extensively investigated and demonstrated as a novel semiconductor photocatalyst for environmental purification.[28−31] The band-gap energy of narrow band-gap semiconductor Bi_2WO_6 is usually referred to as 2.7 eV, which is coincident with its high photocatalytic performance ranging from the ultraviolet to visible region.[32−35] In 2017, Bi_2WO_6 nanoplates were reported to show better radiocatalytic activity in the degradation of aqueous phenol under X-ray irradiation than that of $BiPO_4$ and TiO_2.[24] In addition, the Bi_2WO_6 nanomaterials have been explored for CT imaging-guided synergistic near-infrared light (808 nm) mediated photothermal and photodynamic therapy.[36,37] However, to the best of our knowledge, the application of these high-atomic Bi_2WO_6 semiconductor nanomaterials in radiotherapy has not been previously reported. The X-ray mass attenuation coefficients of Bi (Z = 83) and W (Z = 74) elements at 100 keV are 5.74 and 4.44 cm^2/g, respectively.[2,38] Therefore, we hypothesize that the high-atomic Bi_2WO_6 nanomaterials have the potential to be a novel candidate as a radiosensitizer for radiotherapy. We believe that this study will provide a promising nanotechnology strategy for tumor radiosensitization through simultaneous radiation energy deposition and radiocatalysis.

2. EXPERIMENTAL SECTION

2.1. Materials. Sodium tungstate dihydrate ($Na_2WO_4{\cdot}2H_2O$, 99.0%), bismuth nitrate pentahydrate [$Bi(NO_3)_3{\cdot}5H_2O$, 99.99%], poly(vinylpyrrolidone) (PVP, $M_w \approx 1\,300\,000$), and disodium terephthalate ($C_8H_4Na_2O_4$, 99%) were acquired from Alfa Aesar Reagent Company. Nitric acid (HNO_3, 70%), sodium hydroxide (NaOH, 96.0%), potassium hydroxide (KOH, 99%), and anhydrous ethanol were supplied by Beijing Chemical Reagent Company. Nitrotetrazolium blue chloride (NBT, 98%) was purchased from Sigma-Aldrich. Roswell Park Memorial Institute 1640 (RPMI-1640) and Dulbecco's modified Eagle's medium (DMEM) were obtained from HyClone Company. Cell counting kit-8 (CCK-8), Hoechst 33342, and 2′,7′-dichlorodihydrofluorescein diacetate (DCFH-DA) were purchased from Beyotime Biotechnology. The γ-H2AX antibody was provided by Cell Signaling Technology Company. Deionized water was utilized throughout. All reagents were used as received without further treatment.

2.2. Preparation and Modification of Bi_2WO_6 Nanoplates. The Bi_2WO_6 nanoplates were prepared based on a previously reported hydrothermal method.[29] In a typical process, 10 mmol $Bi(NO_3)_3{\cdot}5H_2O$ (4.95 g) was used as the Bi source and dissolved in 4.5 mL of 20% HNO_3 to obtain solution A, and 5 mmol $Na_2WO_4{\cdot}2H_2O$ (1.67 g) was diffused in 40 mL of deionized water to form solution B. Then, a mixture was formed after the solution A was slowly added into solution B under magnetic stirring at room temperature for 1 h. The pH value of the final milky suspension was adjusted to ∼7.5 by slowly adding KOH solution. Afterward, the suspension was divided and transferred into two 35 mL Teflon-lined autoclaves. After being treated at 180 °C for 2 h, the autoclaves were naturally cooled down to room temperature. The resulting product was collected by centrifugation and rinsed several times with anhydrous ethanol and deionized water and then freeze-dried to obtain a white Bi_2WO_6 powder.

For the modification of Bi_2WO_6 nanoplates, 300 mg of the as-obtained Bi_2WO_6 powders was dispersed in a 20 mL vial containing 5 mL of water in an ultrasonic bath. Then, 5 mL of PVP aqueous solution was added dropwise into the above solution, followed by bath sonication for 2 h at room temperature. Next, PVP−Bi_2WO_6 was collected and washed with deionized water to remove the residual PVP and then redispersed in deionized water and stored in the refrigerator at 4 °C for further use. Some of the as-prepared PVP−Bi_2WO_6 was freeze-dried for the measurements.

2.3. Characterization of Bi_2WO_6 and PVP−Bi_2WO_6 Nanoplates. The morphology and size of the as-prepared Bi_2WO_6 were observed on a transmission electron microscope (TEM, JEM2100-Plus, JEOL). The crystal phase of the samples was measured using X-ray powder diffraction (XRD) analysis on a Bruker D8 Advance diffractometer with Cu Kα radiation (λ = 1.5418 Å). Energy-dispersive X-ray spectroscopy (EDS) was applied to confirm the elemental species and proportion of the sample. X-ray photoelectron spectroscopy (XPS) measurement was performed on a spectrometer (Thermo Scientific ESCALAB 250Xi). Raman spectra were recorded using a Renishaw InVia Raman spectroscopy system with a 514 nm excitation light source. Fourier transform infrared (FT-IR) spectra were recorded using a Bruker EQUINOX55 spectrometer with the KBr pellet technique. UV−vis diffuse reflectance spectra (DRS) were recorded on a UV−vis spectrophotometer (Cary 5000, Agilent) with $BaSO_4$ as the reference. The hydrodynamic diameter and surface charge in water were assessed using a NanoBrook ZetaPALS (Brookhaven) instrument.

2.4. Detection of X-ray-Induced Photocurrent. As previously reported,[18,39] a commercially available miniaturized X-ray tube system (Mini-X, AMPTEK Inc.) was used to measure X-ray-induced photocurrent. The X-ray tube features a 50 kV/80 μA power supply (4 W) and a gold transmission target. Herein, the voltage and current were set to 50 kV and 75 μA for the measurement, respectively. A glass cutter was used to nick a shallow gap on the conducting surface of indium tin oxide (ITO) glass, making it unable to conduct electricity. Then, a little amount of Bi_2WO_6 powder in anhydrous

DOI: 10.1021/acsami.9b03636
ACS Appl. Mater. Interfaces XXXX, XXX, XXX−XXX

ethanol was spread onto the gap of ITO glass and air-dried to fully evaporate ethanol. The vertical distance between the X-ray tube and the ITO glass was ~3 cm. The X-ray-induced current was recorded by a picoammeter in the dark conditions.

2.5. Detection of Reactive Oxygen Species with DCFH-DA. DCFH-DA was selected as the probe for ROS measurement. DCFH-DA can be hydrolyzed to DCFH, which is then oxidized by ROS to form a fluorescent compound, 2′,7′-dichlorofluorescein (DCF).[40,41] First, 0.5 mL of dimethyl sulfoxide containing 12.5 μL of DCFH-DA was added to 2 mL of 0.01 mol/L NaOH in the dark at room temperature. After 30 min, the above reaction was stopped by adding 10 mL of the phosphate buffer (PBS, 25 mmol/L, pH 7.2). The chemically hydrolyzed DCFH solution was kept on the ice and stored in the dark for further use. To measure the production of ROS from Bi_2WO_6 under irradiation, the experiments were divided into four groups: (i) DCFH solution, (ii) DCFH solution with only Bi_2WO_6, (iii) DCFH solution with only X-ray, and (iv) DCFH solution with both Bi_2WO_6 and X-ray irradiation. Notably, the final concentration of Bi_2WO_6 in each group was 10 μg/mL. The mixture solutions were irradiated with an X-ray tube (50 kV, 75 μA) for 10 min. Then, the fluorescence of the irradiated solutions was immediately determined using a Horiba Jobin Yvon Fluorolog-3 spectrofluorometer (λ_{ex} = 488 nm; λ_{em} = 525 nm).

2.6. Measurement of Hydroxyl Radicals with Disodium Terephthalate. The possibility of X-ray-induced $^{\bullet}OH$ generated from Bi_2WO_6 nanoplates was evaluated using terephthalic acid (TA) assay.[42,43] Herein, disodium terephthalate, a nonfluorescent compound, was used as the substitute of TA. In a typical experiment, 11 groups (control, TA, H_2O_2, Bi_2WO_6, TA + H_2O_2, TA + Bi_2WO_6, TA + X-ray, TA + H_2O_2 + X-ray, TA + Bi_2WO_6 + X-ray, TA + H_2O_2 + Bi_2WO_6, and TA + H_2O_2 + Bi_2WO_6 + X-ray) were investigated. In detail, solutions containing TA (0.3 mL, 5 mmol/L), H_2O_2 (0.3 mL, 1 mmol/L), and Bi_2WO_6 (0.3 mL, 100 μg/mL) were added into PBS (1.5 mL, 0.2 mol/L, pH 7.4) and then diluted by deionized water to 3 mL. Some groups were irradiated with an X-ray tube (50 kV, 75 μA) for 10 min. Then, the above solutions were gently shaken overnight at 37 °C in the dark. The fluorescence signal was determined at 435 nm under 315 nm wavelength excitation.

2.7. Detection of Superoxide Radicals with Nitrotetrazolium Blue Chloride. The possibility of X-ray-induced $^{\bullet}O_2^-$ generated from Bi_2WO_6 nanoplates was determined by detecting the absorbance transformation of nitrotetrazolium blue chloride (NBT) at 260 nm. Briefly, 2 mL of 20 μg/mL Bi_2WO_6 aqueous solutions and 2 mL of 30 μg/mL NBT were added into a 5 mL centrifuge tube, and then the mixture solution was ultrasonically dispersed and irradiated with an X-ray tube (50 kV, 75 μA) for 10 min. Then, the solutions were centrifuged (12 000 rpm, 5 min) to remove solid materials. The supernatants in all groups were analyzed by measuring the absorbance at 260 nm on a U-3900 spectrophotometer (HITACHI).

2.8. Cell Culture and in Vitro Cell Viability and Uptake. HeLa cells (human cervical carcinoma) were cultured in RPMI-1640 medium containing 10% (v/v) fetal bovine serum (FBS) and 1% (v/v) penicillin/streptomycin at 37 °C in a humidified 5% CO_2 incubator. Human umbilical vein endothelial cells (HUVECs) were maintained in high-glucose DMEM in the same culture conditions.

To assess the in vitro cytotoxicity, HUVECs cells and HeLa cells were separately seeded in a 96-well plate (5000 cells/well) and cultured for 24 h. Then, cells were incubated with different concentrations of PVP−Bi_2WO_6 nanoplates (100 μL/well, 0, 3.13, 6.25, 12.5, 25, 50, 100, 200, and 400 μg/mL) for another 24 h. The cellular viability was evaluated by the standard CCK-8 assay.

The cellular uptake of PVP−Bi_2WO_6 nanoplates was performed as follows: HeLa cells were planted in a 6-well plate (10×10^4 cells/well) with a coverslip placed at the bottom and cultured in growth medium until cells adhered to the coverslip. After 24 h incubation, the cells were then incubated with 2 mL of culture medium containing PVP−Bi_2WO_6 (100 μg/mL) at 37 °C for 12 and 24 h. Next, the culture medium was discarded and the well plate was rinsed three times with PBS. Then, the cellular nucleus was stained with Hoechst 33342 for 15 min. The coverslips were then rinsed three times with PBS and fixed by antifade mounting medium onto a glass slide. Finally, the light scattering images were collected on an inverted fluorescence microscope (IX73, Olympus), which is coupled with a Nikon dark-field condenser.

2.9. Determination of Reactive Oxygen Species Generation in Cells. The DCFH-DA probe was selected to measure the intracellular ROS generation. HeLa cells were seeded in a confocal dish (5×10^4 cells/well) with complete medium for 24 h. Afterward, cells were divided into four groups: (i) control, (ii) PVP−Bi_2WO_6 alone, (iii) X-ray alone, and (iv) PVP−Bi_2WO_6 with X-ray irradiation. When cells had grown to 80% in plates, the cells in the groups (ii) and (iv) were then incubated with PVP−Bi_2WO_6 (100 μg/mL) for 24 h. Afterward, the wells were rinsed three times with PBS and incubated with 1 mL of DCFH-DA (10 mmol/L) in Hoechst 33342 (1:1000, v/v) for 15 min. Then, the cells in the groups (iii) and (iv) were seeded in 1 mL of PBS and X-ray irradiated (50 kV, 75 μA) for 10 min after being rinsed with PBS. Finally, the level of intracellular ROS was monitored by confocal laser scanning microscopy (Nikon A1).

2.10. In Vitro Colony Formation Assay. The clonogenic assay was used to evaluate the radiosensitizing effect of Bi_2WO_6 based on the previously reported method.[18,44−46] HeLa cells were seeded in a 6-well plate (2000 cells/well) for 24 h. After being incubated with PVP−Bi_2WO_6 (100 μg/mL) for 6 h, cells were washed and X-ray (50 kV, 75 μA) irradiated for 30 s. Then, the cells both in the control and irradiated groups were cultured with 2 mL of fresh medium for 10−20 days until the formation of a visible colony. Next, the culture medium was discarded and the plate was rinsed three times with PBS. Afterward, HeLa cells were fixed by 4% paraformaldehyde at room temperature for 15 min and then rinsed three times with PBS and stained with Giemsa dye for another 20 min. Finally, the 6-well plate was rinsed with water and the colonies were counted manually.

2.11. In Vitro DNA Double-Strand Break Assay. To assess DNA double-strand breaks, HeLa cells were planted in a 24-well plate with a coverslip at a density of 3×10^4 cells/well and incubated for 24 h. The experiments were performed on four groups: (i) control, (ii) PVP−Bi_2WO_6 alone, (iii) X-ray alone, and (iv) PVP−Bi_2WO_6 with X-ray irradiation. Then, the cells in the groups (ii) and (iv) were treated with PVP−Bi_2WO_6 (100 μg/mL). After incubation for 24 h, the cells in the groups (iii) and (iv) were X-ray irradiated for 10 min (50 kV, 75 μA). After incubation for another 3 h, the immunofluorescence staining of γ-H2AX was carried out. First, the cells were fixed with 4% paraformaldehyde for 10 min and washed three times with PBS. Then, 0.2% Triton X-100 was used to penetrate cells for 10 min. Next, blocking buffer (1% BSA in PBS solution) was added to the cells for another 1 h at room temperature. Afterward, cells were incubated with γ-H2AX antibody overnight at 4 °C. Next, the cells were treated with Cy3-labeled goat anti-rabbit IgG (H + L) secondary antibody for 1 h. After removing the excess antibody and washing coverslips, the cell nucleus was stained with Hoechst 33342 and then imaged on a confocal microscope.

2.12. In Vivo Antitumor Efficacy of Radiotherapy. Female BALB/c nude mice were obtained from Cancer Institute and Hospital, Chinese Academy of Medical Sciences. All animal studies were approved under the guidelines set by the Chinese Academy of Sciences Key Laboratory for Biomedical Effects of Nanomaterials and Nanosafety.

To set up the animal model, a total of 1×10^6 HeLa cells were injected subcutaneously into the right hind legs of the BALB/c mouse. When the tumor volume reached ~50 mm^3, the mice were randomly divided into four groups (n = 4): (i) control, (ii) PVP−Bi_2WO_6, (iii) X-ray, and (iv) X-ray + PVP−Bi_2WO_6. The tumor-bearing mice of groups (ii) and (iv) were intratumorally (i.t.) injected with 25 μL of PVP−Bi_2WO_6 (2 mg/mL), and the groups (iii) and (iv) were exposed to X-ray by a medical linear accelerator (6 Gy). After treatment, the mice were normally bred and the body weight and tumor size were recorded every other day. The tumor volume was estimated according to the formula: $V = ab^2/2$, where a and b are tumor length and width, respectively. The mice in each group were sacrificed until the end of the experiment. The tumor and major

DOI: 10.1021/acsami.9b03636
ACS Appl. Mater. Interfaces XXXX, XXX, XXX−XXX

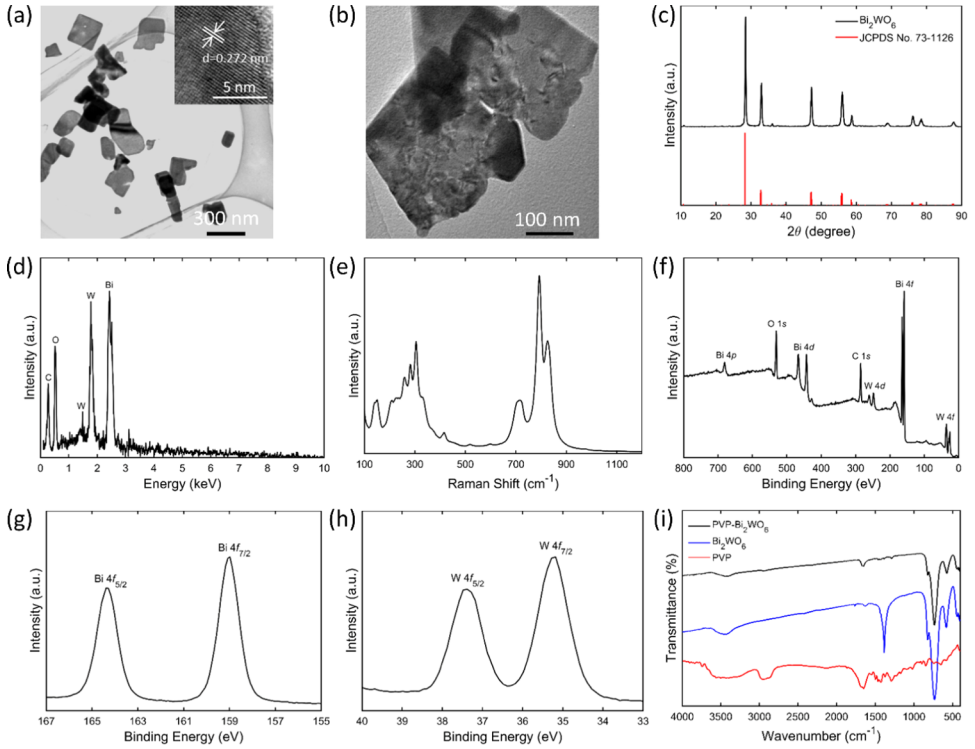

Figure 1. Physicochemical characterization of Bi_2WO_6 nanoplates. (a, b) TEM images, (c) powder XRD patterns, (d) EDS analysis, and (e) Raman spectra of the as-prepared Bi_2WO_6 nanoplates. XPS of (f) Bi_2WO_6 nanoplates, (g) Bi 4f, and (h) W 4f. (i) FT-IR spectra of PVP, Bi_2WO_6, and PVP−Bi_2WO_6. a.u., arbitrary units.

organs (including heart, spleen, lung, liver, and kidney) were weighed and stained to assess the therapeutic efficacy of each group.

2.13. Blood Hematology and Biochemistry Analyses. The blood hematology and biochemistry analyses were conducted at the Animal Department of Peking University Medical Laboratory. The tumors and major organs were fixed with 4% paraformaldehyde and then cryosectioned as slices after being embedded in paraffin. Finally, the histological sections were co-stained with hematoxylin and eosin (H&E) and imaged on an optical microscope.

2.14. Statistical Analysis. The collected experimental data were analyzed using Student's *t* test. The results were presented as mean ± standard deviation of three independent experiments. *P* values of less than 0.001 (***), 0.001−0.01 (**), and 0.01−0.05 (*) were considered to be significant.

3. RESULTS AND DISCUSSION

3.1. Synthesis and Characterization of PVP−Bi_2WO_6 Nanoplates. The Bi_2WO_6 nanoplates were successfully synthesized by a simple one-pot hydrothermal method according to the previous method with a few modifications.[29] As evidenced by TEM (Figure 1a,b), the as-prepared Bi_2WO_6 presented a thin lamellar morphology with a length of ∼240 nm. The high-resolution TEM image (Figures 1a and S1) presents legible lattice fringes with the lattice spacing of 0.272 nm, which is consistent with the (020) plane of orthorhombic Bi_2WO_6. The thickness of the as-prepared Bi_2WO_6 nanoplates was examined by atomic force microscopy (AFM, Figure S2) and estimated to be about 5 nm. XRD was used to study the crystal structure of the as-prepared samples. As shown in Figure 1c, all of the characteristic peaks of the as-prepared samples matched well with those of the standard orthorhombic Bi_2WO_6 phase (JCPDS no. 73-1126). Energy-dispersive X-ray spectroscopy (EDS) (Figure 1d) and Raman spectrum (Figure 1e) analysis of the as-obtained samples further confirmed the successful preparation of Bi_2WO_6.[47,48] The chemical compositions of the as-prepared Bi_2WO_6 nanoplates were analyzed using XPS (Figure 1f). Figure 1g,h presents the high-resolution Bi 4f and W 4f XPS spectra of the Bi_2WO_6 nanoplates. According to the previous reports,[31,49−51] the shoulder peaks of a doublet splitting at the binding energies of 164.38 and 158.98 eV were assigned to Bi $4f_{5/2}$ and Bi $4f_{7/2}$, whereas 37.38 and 35.18 eV were ascribed to W $4f_{5/2}$ and W $4f_{7/2}$, respectively. The high-resolution O 1s spectrum is shown in the Supporting Information (Figure S3). The results of XPS indicated that the oxidation states of Bi and W in the as-prepared Bi_2WO_6 nanoplates are Bi^{3+} and W^{6+}, respectively.

To improve the water solubility and biocompatibility, the as-prepared Bi_2WO_6 nanoplates were subsequently functionalized with poly(vinylpyrrolidone) (PVP) through the physical absorption. As presented in the FT-IR spectrum (Figure 1i), the peaks at 1651 and 1296 cm^{-1} could be, respectively, assigned to C═O and C−N, indicating the successful coating of PVP on the surface of the Bi_2WO_6 nanoplates. Thermogravimetric analysis (TGA) was carried out using a thermal gravimetric analyzer with a heating rate of 20 °C/min from room temperature to 900 °C in a N_2 atmosphere. The PVP−Bi_2WO_6 samples show a weight loss of 11.34% with heating to 900 °C (Figure S4). The average hydrodynamic diameter of PVP−Bi_2WO_6 was ∼295 nm, determined through dynamic light scatting (DLS, Figure S5). The zeta potential of PVP−Bi_2WO_6 in water was around −17.96 mV (Figure S6). In addition, PVP−Bi_2WO_6 was found to be well dispersed in water, PBS, RPMI-1640, and FBS for 12 h (Figure S7).

3.2. X-ray Radiocatalytic Activity of PVP−Bi_2WO_6 Nanoplates. Bi_2WO_6 nanoparticles have been demonstrated to be novel photocatalysts with high photocatalytic activity in the degradation of organic dyes over the last decades.[28−31]

DOI: 10.1021/acsami.9b03636
ACS Appl. Mater. Interfaces XXXX, XXX, XXX−XXX

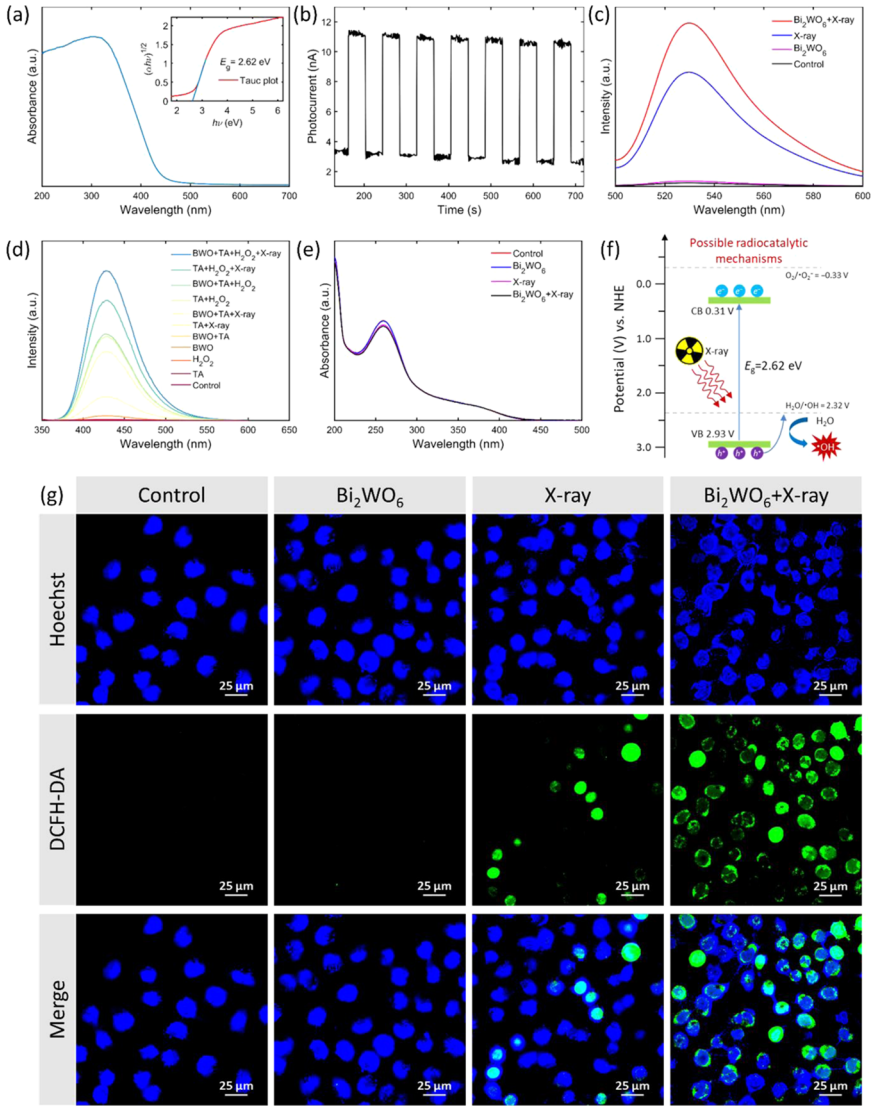

Figure 2. X-ray-induced radiocatalytic activity and ROS generation from Bi_2WO_6 nanoplates. (a) Diffuse reflectance ultraviolet−visible spectra of Bi_2WO_6 nanoplates; insets display the Tauc plots. (b) Photocurrent characteristics of the as-prepared Bi_2WO_6 semiconductors, recorded with or without X-ray irradiation (50 kV, 75 μA, 10 min). (c) Fluorescence spectra of ROS measurement by DCFH-DA. (d) Fluorescence spectra of $^{\bullet}OH$ measurement by disodium terephthalate. BWO, Bi_2WO_6. (e) Degradation of NBT by $^{\bullet}O_2^-$ with and without X-ray irradiation. (f) Possible X-ray-induced radiocatalytic mechanisms of Bi_2WO_6 semiconductors. (g) Fluorescence images for ROS generation in HeLa cells stained by Hoechst 33342 and DCFH-DA after various treatments. The scale bar is 25 μm.

However, the radiocatalytic performance of Bi_2WO_6 semiconductor nanoplates has not been clearly ascertained till now. To promote the ROS production in radiotherapy, we made the first attempt to design the Bi_2WO_6 semiconductor nanoplates containing high-Z elements to increase the deposition of X-ray energy and subsequently enhance the ROS generation via the X-ray-mediated radiocatalytic process.

First, the optical band gap of Bi_2WO_6 was measured by ultraviolet−visible diffuse reflectance spectroscopy (DRS). As depicted in Figure 2a, the absorption edge of the as-prepared Bi_2WO_6 was located at approximately 460 nm. Since Bi_2WO_6 is an indirect band-gap semiconductor,[34] the band-gap energy (E_g) of Bi_2WO_6 was estimated from the Tauc plots of $(\alpha hv)^{1/2}$ versus photon energy (hv), where α, h, and v are the absorption coefficient, Planck's constant, and the light frequency, respectively.[28,52] Thus, the E_g of the as-prepared Bi_2WO_6 nanoplates could be calculated as ~2.62 eV, which is consistent with that in previous reports.[33,52] Afterward, we first detected the photocurrent generated from Bi_2WO_6 semiconductors under X-ray excitation. As presented in Figure 2b, the photocurrents display a rapid response with the X-ray turn on/off, directly indicating the efficient separation of electron/hole (e^-/h^+) in the air environment. The result demonstrated that Bi_2WO_6 nanoplates possess good X-ray-responsive properties.

In aqueous solution or biological environment, the radio-excited electrons and holes in the radiocatalytic process are able to initiate the redox chemical reactions, which are accompanied by ROS generation. Encouraged by the formation of X-ray-triggered photocurrent, we then tested the ROS generated from Bi_2WO_6 under X-ray irradiation in water medium by a nonfluorescent molecule, DCFH-DA. DCFH-DA can be hydrolyzed to DCFH, which is then oxidized by ROS to form fluorescent 2′,7′-dichlorofluorescein (DCF).[40] As shown in Figure 2c, after X-ray irradiation, the fluorescence signals of the PVP−Bi_2WO_6 group were obviously

DOI: 10.1021/acsami.9b03636
ACS Appl. Mater. Interfaces XXXX, XXX, XXX−XXX

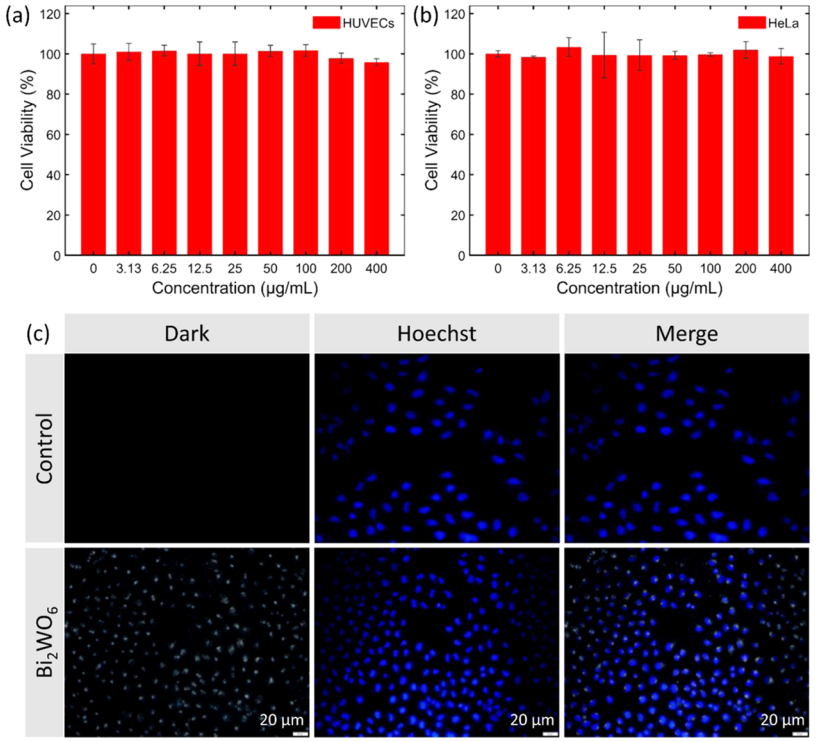

Figure 3. In vitro cytotoxicity and cellular uptake evaluation of Bi_2WO_6 nanoplates. The viability of (a) HUVECs and (b) HeLa cells incubated with different concentrations of PVP−Bi_2WO_6 nanoplates for 24 h. (c) Dark-field optical microscopy images of HeLa cells incubated with 100 μg/mL PVP−Bi_2WO_6 nanoplates for 24 h. The scale bar is 20 μm.

increased in contrast to those of other groups. It is noteworthy that the ROS production in the group treated with X-ray alone was also higher than that of the control group, demonstrating the efficient radiolysis of H_2O by X-ray. These results indicated that the ROS generation not only originated from the radiolysis of H_2O molecules but was also enhanced by Bi_2WO_6-mediated radiocatalysis.

It is generally accepted that some kinds of oxidative species (e.g., $^{\bullet}OH$ and $^{\bullet}O_2^-$) can be produced in a photocatalytic process.[53] According to some previous studies,[31,52] $^{\bullet}OH$ and $^{\bullet}O_2^-$ species can be generated in the degradation of organic dyes during Bi_2WO_6 photocatalysis. However, it is not clear whether the $^{\bullet}OH$ and $^{\bullet}O_2^-$ are also produced in the radiocatalytic process mediated by Bi_2WO_6 semiconductor nanoplates. On the one hand, since an $^{\bullet}OH$ radical is a representative cytotoxic radical species in ROS family and may be generated in the radiocatalytic process, we first measured the production of $^{\bullet}OH$ using sodium terephthalate as the probe. Sodium terephthalate can react with $^{\bullet}OH$ and yield an aromatic hydroxylated fluorescent product (sodium 2-hydroxyterephthalate) whose maximum fluorescence emission peak is ~435 nm.[40] Therefore, we could determine the existence of $^{\bullet}OH$ by monitoring the fluorescence changes of sodium 2-hydroxyterephthalate. After X-ray irradiation and 12 h reaction, the highest fluorescence intensity at 435 nm was observed in the PVP−Bi_2WO_6- and H_2O_2-treated groups (Figure 2d), indicating the presence of $^{\bullet}OH$ radicals. Herein, from the point of view of the photocatalytic mechanisms of semiconductors, the production of $^{\bullet}OH$ may be enhanced by the reaction of holes (h^+) with the surrounding H_2O molecule adsorbed on the surface of Bi_2WO_6 nanoplates [e.g., $H_2O + h^+ \rightarrow {}^{\bullet}OH + H^+$, $\Delta E^0(H_2O/{}^{\bullet}OH)$ = 2.32 V, pH 7, ref 54] as well. On the other hand, due to the reason that the NBT can be specifically reduced by $^{\bullet}O_2^-$ to form the insoluble purple formazan,[46,53] displaying an absorbance change at 260 nm, the possibility of X-ray-induced $^{\bullet}O_2^-$ generated from Bi_2WO_6 nanoplates was determined by NBT transformation. As it can be seen in Figure 2e, in contrast, there was only a slight absorbance decrease of NBT at 260 nm in the X-ray treated groups. Moreover, the absorbance values in both X-ray alone and X-ray + Bi_2WO_6 added groups were almost coincident, to some extent indicating the absence of $^{\bullet}O_2^-$ in the Bi_2WO_6-mediated radiocatalytic process. Generally, the type of oxidative species generated during radiocatalysis is determined by the semiconductors' conduction and valence band edge energies.[54] According to previous references,[33,34] the E_{CB} and E_{VB} of the as-prepared Bi_2WO_6 nanoplates ($E_g \approx 2.62$ eV) could be determined to be ~0.31 and ~2.93 V (vs the normal hydrogen electrode), respectively, as shown in Figure 2f. Therefore, unlike the traditional mechanisms, the conduction band electrons of Bi_2WO_6 are not strong enough to generate $^{\bullet}O_2^-$ due to the thermodynamic limitations [$\Delta E^0(O_2/{}^{\bullet}O_2^-)$ = −0.33 V, pH 7, ref 33]. In conclusion, we surmised that the main type of oxidative species generated by Bi_2WO_6 from the radiocatalytic process may be $^{\bullet}OH$, thereby contributing to the radiosensitization.

Then, we examined the ROS generation ability of PVP−Bi_2WO_6 under X-ray irradiation at the cellular level. ROS generation was confirmed by DCF fluorescence signal detection in live cells using confocal laser scanning. As shown in Figure 2g, brightest green fluorescence signals were observed only in HeLa cells treated with both PVP−Bi_2WO_6 and X-ray irradiation, whereas only weak fluorescence signals can be recorded in control or PBS groups without X-ray. This suggests that high intracellular ROS concentration was generated from the interaction of Bi_2WO_6 with X-ray

DOI: 10.1021/acsami.9b03636
ACS Appl. Mater. Interfaces XXXX, XXX, XXX−XXX

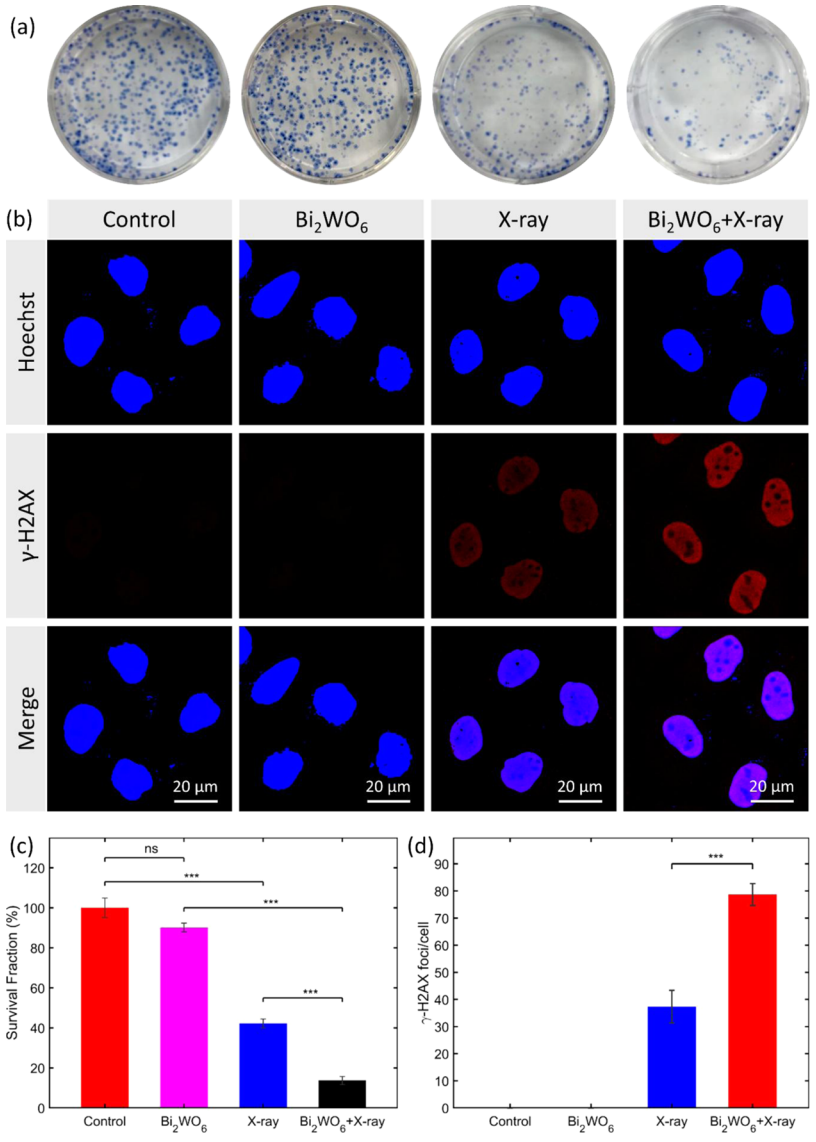

Figure 4. Radiosensitization of Bi_2WO_6 nanoplates in vitro. (a) Representative photographs of colony formation of HeLa cells after treatment with 100 μg/mL PVP−Bi_2WO_6 nanoplates and with or without X-ray irradiation (50 kV, 75 μA, 30 s). (b) γ-H2AX assays of DNA damage after various treatments. The scale bar is 20 μm. (c) Corresponding survival fraction of colony formation assay after various treatments. (d) Corresponding number of γ-H2AX after different treatments. $n = 3$. P values were based on Student's t test: $^*P < 0.05$, $^{**}P < 0.01$, $^{***}P < 0.001$.

irradiation. Therefore, the as-prepared Bi_2WO_6 has the potential to become a radiosensitizer for cancer radiotherapy.

3.3. Cytotoxicity and Cellular Uptake of PVP−Bi_2WO_6 Nanoplates. Next, the in vitro cytotoxicity profiles and cellular uptake of Bi_2WO_6 were studied to meet the requirements of the diagnostic and therapeutic applications. The relative viabilities of HUVECs and HeLa cells incubated with PVP−Bi_2WO_6 nanoplates were assessed using the standard CCK-8 assay.

As shown in Figure 3a,b, the PVP-modified Bi_2WO_6 showed negligible cytotoxicity on cell viability (>90%) even at the highest concentration (400 μg/mL). The results are coincident with those of the previous studies[36,37] and further indicate that PVP−Bi_2WO_6 has good biocompatibility for biomedical applications.

Additionally, since the sufficient accumulation of nanoparticles in cancer cells is critical for their therapeutic behaviors, the in vitro cellular uptake of PVP−Bi_2WO_6 nanoplates in HeLa cells was also tested. As a particularly useful imaging tool, dark-field scattering microscopy was utilized to visualize Bi_2WO_6 nanoplates.[55−57] After incubation with 100 μg/mL Bi_2WO_6 nanoplates for 24 h, an obvious signal enhancement was observed (Figures 3c and S8), whereas the control group without Bi_2WO_6 nanoplates showed no obvious scattering signals, suggesting that the as-prepared Bi_2WO_6 could be effectively internalized into the cells.

3.4. Radiosensitization of PVP−Bi_2WO_6 Nanoplates in Vitro. After demonstrating the good biocompatibility and the efficient cellular uptake of Bi_2WO_6, we then evaluated the in vitro survival of cells by the clonogenic assay, which is a commonly used method for evaluating cell reproductive death after treatment with ionizing radiation.[58] Hela cells were cultured in a 6-well plate and treated with PVP−Bi_2WO_6 (100 μg/mL) and X-ray irradiation to form colonies in ~2 weeks. As depicted in Figure 4a,c, the colony formation in HeLa cells treated with PVP−Bi_2WO_6 or X-ray alone decreased to ~90.2 and ~42.2%, respectively, whereas that in the Bi_2WO_6- and X-ray-treated groups markedly decreased to ~13.7%. This

DOI: 10.1021/acsami.9b03636
ACS Appl. Mater. Interfaces XXXX, XXX, XXX−XXX

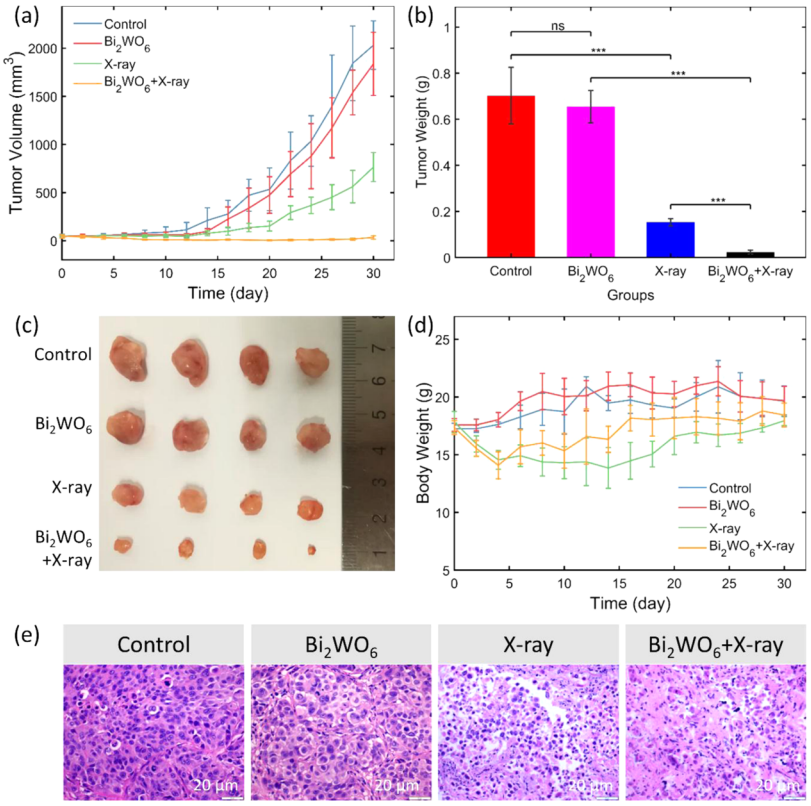

Figure 5. In vivo radiotherapy efficacy of Bi_2WO_6 nanoplates. (a) Tumor growth curves of different groups of mice during 30 days treatment. (b) Tumor weights and (c) photos of different groups of mice after different treatments. (d) Body weights of different groups of mice during 30 days treatment. (e) Representative microscopy images of H&E-stained tumor slices collected from different groups of mice. The scale bar is 20 μm. n = 4. P values were based on Student's t test: *P < 0.05, **P < 0.01, ***P < 0.001.

outcome further indicated that PVP−Bi_2WO_6 has the potential to be a radiosensitizer for cancer cell killing.

The radiosensitization of PVP−Bi_2WO_6 was further confirmed by probing DNA double-strand breaks, which are unusually caused by high ROS level. A γ-H2AX staining technique was utilized to evaluate the double-strand breaks in DNA under various conditions. Consistent with the results of the clonogenic assay, significant γ-H2AX fluorescence was observed in the nuclei of HeLa cells in the Bi_2WO_6- and X-ray-treated groups, whereas no obvious double-strand breaks were found in the group of PVP−Bi_2WO_6 or X-ray (Figure 4b,d). The results demonstrated that HeLa cells treated with PVP−Bi_2WO_6 and X-ray showed severe DNA damage. Therefore, PVP−Bi_2WO_6 can improve radiation-induced DNA damage and thus inhibit the growth of cancer cells, realizing X-ray-mediated radiosensitization.

3.5. Radiotherapy of PVP−Bi_2WO_6 Nanoplates in Vivo. Motivated by the outcomes in vitro, we then investigated the in vivo radiotherapy of Bi_2WO_6 nanoplates by in situ intratumoral administration on the animal model. First, we explored the tumor CT imaging ability of the Bi_2WO_6 nanoplates. When the tumor-bearing mice were i.t. injected with the as-prepared PVP−Bi_2WO_6 solutions (20 μL, 25 mg/mL) and subsequently imaged at different time points, strong CT signals in the tumor region could be observed (Figure S9). It indicated an efficient accumulation of PVP−Bi_2WO_6 nanoplates in the tumor. Next, the tumor-bearing BALB/c nude mice were randomly divided into four groups (n = 4). After 0.5 h post injection of PVP−Bi_2WO_6 solution (2 mg/mL, 25 μL for each mouse) intratumorally, the mice were exposed to 6 Gy of X-ray radiation. During 4 weeks after treatment, the body weight and tumor size of the mice in each group were recorded. As depicted in Figure 5a, the control or PVP−Bi_2WO_6-only-treated group witnessed a rapid increase in tumor size. Therefore, it is simply hard to eradicate tumors sufficiently by treating with PVP−Bi_2WO_6. In contrast with radiotherapy alone, the PVP−Bi_2WO_6 + X-ray group exhibited significant tumor growth inhibition performance. The antitumor effects in vivo were also firmly supported by the tumor weights and histology of tumor slices in Figure 5b,c,e, indeed demonstrating the radiosensitization of PVP−Bi_2WO_6 nanoplates. We additionally evaluated the potential toxicity of PVP−Bi_2WO_6 nanoplates by H&E staining and hematology analysis. As depicted in Figures 5d and S10−S12, these results suggested that no noticeable toxicities in vivo or organ damage induced by the as-prepared PVP−Bi_2WO_6 nanoplates was observed at least at our tested doses within 30 days after radiotherapy treatment. However, from the point of view of biosafety, the potential long-term toxicity of Bi_2WO_6 to animals should be subjected to more careful studies, to enable further use of this emerging Bi_2WO_6 nanomaterial in the biomedicine field.

4. CONCLUSIONS

We prepared PVP-modified Bi_2WO_6 nanoplates with good solubility and biocompatibility through a facile hydrothermal method and found that they have the potential to be novel radiosensitizers for the enhancement of radiotherapy for the first time. The as-obtained high-Z Bi_2WO_6 semiconductor nanoplates not only showed obvious X-ray excited photo-

DOI: 10.1021/acsami.9b03636
ACS Appl. Mater. Interfaces XXXX, XXX, XXX−XXX

current but also exhibited significant radiocatalytic activity under X-ray irradiation, giving rise to the effective separation of e^-/h^+ pairs and subsequently promoting the generation of cytotoxic ROS, especially $^{\bullet}OH$. The γ-H2AX and clonogenic assays demonstrated that PVP−Bi_2WO_6 could efficiently increase X-ray-induced intracellular DNA damages and colony formations. These versatile features endowed PVP−Bi_2WO_6 nanoplates with enhanced radiotherapy efficacy in animal models. In addition, Bi_2WO_6 nanoplates could also serve as good X-ray CT imaging contrast agents. These findings may provide an alternative nanotechnology strategy for tumor radiosensitization through simultaneous radiation energy deposition and radiocatalysis.

■ ASSOCIATED CONTENT

Supporting Information

The Supporting Information is available free of charge on the ACS Publications website at DOI: 10.1021/acsami.9b03636.

High-resolution TEM images; AFM image; high-resolution XPS of O 1s; TGA; DLS of PVP−Bi_2WO_6; ζ-potentials of PVP−Bi_2WO_6; dispersity of PVP−Bi_2WO_6 in water, PBS, RPMI-1640 culture, and FBS; CT images of a tumor; blood biochemistry and hematology analyses; H&E-stained images (PDF)

■ AUTHOR INFORMATION

Corresponding Authors

*E-mail: zjgu@ihep.ac.cn (Z.G.).
*E-mail: qwang@sdust.edu.cn (Q.W.).

ORCID

Zhanjun Gu: 0000-0003-3717-2423

Author Contributions

‖Y.Z. and L.G. contributed equally to this work.

Notes

The authors declare no competing financial interest.

■ ACKNOWLEDGMENTS

This work was supported by the National Basic Research Programs of China (2016YFA0201600), the National Natural Science Foundation of China (nos. 51822207, 51772292, 31571015, and 11621505), Youth Innovation Promotion Association CAS (2013007), Taishan Scholarship Project of Shandong, China (no. TSHW20130956), and the Natural Science Foundation of Shandong Province (no. ZR2017MA013).

■ REFERENCES

(1) Thariat, J.; Hannoun-Levi, J.-M.; Sun Myint, A.; Vuong, T.; Gérard, J.-P. Past, Present, and Future of Radiotherapy for the Benefit of Patients. *Nat. Rev. Clin. Oncol.* **2013**, *10*, 52−60.

(2) Gong, L.; Xie, J.; Zhu, S.; Gu, Z.; Zhao, Y. Application of Multifunctional Nanomaterials in Tumor Radiosensitization. *Acta Phys.-Chim. Sin.* **2018**, *34*, 140−167.

(3) Wang, H.; Mu, X.; He, H.; Zhang, X.-D. Cancer Radiosensitizers. *Trends Pharmacol. Sci.* **2018**, *39*, 24−48.

(4) Xie, J.; Gong, L.; Zhu, S.; Yong, Y.; Gu, Z.; Zhao, Y. Emerging Strategies of Nanomaterial-Mediated Tumor Radiosensitization. *Adv. Mater.* **2019**, *31*, No. 1802244.

(5) Kwatra, D.; Venugopal, A.; Anant, S. Nanoparticles in Radiation Therapy: A Summary of Various Approaches to Enhance Radiosensitization in Cancer. *Transl. Cancer Res.* **2013**, *2*, 330−342.

(6) Paunesku, T.; Gutiontov, S.; Brown, K.; Woloschak, G. E. Radiosensitization and Nanoparticles. In *Nanotechnology-Based Precision Tools for the Detection and Treatment of Cancer*; Mirkin, C. A.; Meade, T. J.; Petrosko, S. H.; Stegh, A. H., Eds.; Springer International Publishing: Cham, 2015; pp 151−171.

(7) Chen, H.; Gu, Z.; An, H.; Chen, C.; Chen, J.; Cui, R.; Chen, S.; Chen, W.; Chen, X.; Chen, X.; Chen, Z.; Ding, B.; Dong, Q.; Fan, Q.; Fu, T.; Hou, D.; Jiang, Q.; Ke, H.; Jiang, X.; Liu, G.; Li, S.; Li, T.; Liu, Z.; Nie, G.; Ovais, M.; Pang, D.; Qiu, N.; Shen, Y.; Tian, H.; Wang, C.; Wang, H.; Wang, Z.; Xu, H.; Xu, J.-F.; Yang, X.; Zhu, S.; Zheng, X.; Zhang, X.; Zhao, Y.; Tan, W.; Zhang, X.; Zhao, Y. Precise Nanomedicine for Intelligent Therapy of Cancer. *Sci. China: Chem.* **2018**, *61*, 1503−1552.

(8) Lusic, H.; Grinstaff, M. W. X-ray-Computed Tomography Contrast Agents. *Chem. Rev.* **2013**, *113*, 1641−1666.

(9) Hernández-Rivera, M.; Kumar, I.; Cho, S. Y.; Cheong, B. Y.; Pulikkathara, M. X.; Moghaddam, S. E.; Whitmire, K. H.; Wilson, L. J. High-Performance Hybrid Bismuth−Carbon Nanotube Based Contrast Agent for X-ray CT Imaging. *ACS Appl. Mater. Interfaces* **2017**, *9*, 5709−5716.

(10) Kobayashi, K.; Usami, N.; Porcel, E.; Lacombe, S.; Le Sech, C. Enhancement of Radiation Effect by Heavy Elements. *Mutat. Res., Rev. Mutat. Res.* **2010**, *704*, 123−131.

(11) Chow, J. C. L. Characteristics of Secondary Electrons from Irradiated Gold Nanoparticle in Radiotherapy. In *Handbook of Nanoparticles*; Aliofkhazraei, M., Ed.; Springer International Publishing: Cham, 2015; Chapter 10-1, pp 1−18.

(12) Juzenas, P.; Chen, W.; Sun, Y.-P.; Coelho, M. A. N.; Generalov, R.; Generalova, N.; Christensen, I. L. Quantum Dots and Nanoparticles for Photodynamic and Radiation Therapies of Cancer. *Adv. Drug Delivery Rev.* **2008**, *60*, 1600−1614.

(13) Butterworth, K. T.; McMahon, S. J.; Currell, F. J.; Prise, K. M. Physical Basis and Biological Mechanisms of Gold Nanoparticle Radiosensitization. *Nanoscale* **2012**, *4*, 4830−4838.

(14) Schuemann, J.; Berbeco, R.; Chithrani, D. B.; Cho, S. H.; Kumar, R.; McMahon, S. J.; Sridhar, S.; Krishnan, S. Roadmap to Clinical Use of Gold Nanoparticles for Radiation Sensitization. *Int. J. Radiat. Oncol., Biol., Phys.* **2016**, *94*, 189−205.

(15) Rosa, S.; Connolly, C.; Schettino, G.; Butterworth, K. T.; Prise, K. M. Biological Mechanisms of Gold Nanoparticle Radiosensitization. *Cancer Nanotechnol.* **2017**, *8*, 2.

(16) Ma, M.; Huang, Y.; Chen, H.; Jia, X.; Wang, S.; Wang, Z.; Shi, J. Bi_2S_3-Embedded Mesoporous Silica Nanoparticles for Efficient Drug Delivery and Interstitial Radiotherapy Sensitization. *Biomaterials* **2015**, *37*, 447−455.

(17) Wang, Y.; Wu, Y.; Liu, Y.; Shen, J.; Lv, L.; Li, L.; Yang, L.; Zeng, J.; Wang, Y.; Zhang, L. W.; Li, Z.; Gao, M.; Chai, Z. BSA-Mediated Synthesis of Bismuth Sulfide Nanotheranostic Agents for Tumor Multimodal Imaging and Thermoradiotherapy. *Adv. Funct. Mater.* **2016**, *26*, 5335−5344.

(18) Guo, Z.; Zhu, S.; Yong, Y.; Zhang, X.; Dong, X.; Du, J.; Xie, J.; Wang, Q.; Gu, Z.; Zhao, Y. Synthesis of BSA-Coated BiOI@Bi_2S_3 Semiconductor Heterojunction Nanoparticles and Their Applications for Radio/Photodynamic/Photothermal Synergistic Therapy of Tumor. *Adv. Mater.* **2017**, *29*, No. 1704136.

(19) Zhang, X.-D.; Chen, J.; Min, Y.; Park, G. B.; Shen, X.; Song, S.-S.; Sun, Y.-M.; Wang, H.; Long, W.; Xie, J.; Gao, K.; Zhang, L.; Fan, S.; Fan, F.; Jeong, U. Metabolizable Bi_2Se_3 Nanoplates: Biodistribution, Toxicity, and Uses for Cancer Radiation Therapy and Imaging. *Adv. Funct. Mater.* **2014**, *24*, 1718−1729.

(20) Song, G.; Liang, C.; Yi, X.; Zhao, Q.; Cheng, L.; Yang, K.; Liu, Z. Perfluorocarbon-Loaded Hollow Bi_2Se_3 Nanoparticles for Timely Supply of Oxygen under Near-Infrared Light to Enhance the Radiotherapy of Cancer. *Adv. Mater.* **2016**, *28*, 2716−2723.

(21) Du, J.; Gu, Z.; Yan, L.; Yong, Y.; Yi, X.; Zhang, X.; Liu, J.; Wu, R.; Ge, C.; Chen, C.; Zhao, Y. Poly(Vinylpyrollidone)- and Selenocysteine-Modified Bi_2Se_3 Nanoparticles Enhance Radiotherapy Efficacy in Tumors and Promote Radioprotection in Normal Tissues. *Adv. Mater.* **2017**, *29*, No. 1701268.

(22) Cheng, L.; Liu, J.; Gu, X.; Gong, H.; Shi, X.; Liu, T.; Wang, C.; Wang, X.; Liu, G.; Xing, H.; Bu, W.; Sun, B.; Liu, Z. PEGylated WS_2

DOI: 10.1021/acsami.9b03636
ACS Appl. Mater. Interfaces XXXX, XXX, XXX−XXX

Nanosheets as a Multifunctional Theranostic Agent for in Vivo Dual-Modal CT/Photoacoustic Imaging Guided Photothermal Therapy. *Adv. Mater.* **2014**, *26*, 1886−1893.
(23) Yong, Y.; Cheng, X.; Bao, T.; Zu, M.; Yan, L.; Yin, W.; Ge, C.; Wang, D.; Gu, Z.; Zhao, Y. Tungsten Sulfide Quantum Dots as Multifunctional Nanotheranostics for in Vivo Dual-Modal Image-Guided Photothermal/Radiotherapy Synergistic Therapy. *ACS Nano* **2015**, *9*, 12451−12463.
(24) Sahu, S. P.; Cates, E. L. X-ray Radiocatalytic Activity and Mechanisms of Bismuth Complex Oxides. *J. Phys. Chem. C* **2017**, *121*, 10538−10545.
(25) Serpone, N.; Emeline, A. V. Suggested Terms and Definitions in Photocatalysis and Radiocatalysis. *Int. J. Photoenergy* **2002**, *4*, 91−131.
(26) Hoertz, P. G.; Magnus-Aryitey, D.; Gupta, V.; Norton, C.; Doorn, S.; Ennis, T. Photocatalytic and Radiocatalytic Nanomaterials for the Degradation of Organicspecies. *Radiat. Phys. Chem.* **2013**, *84*, 51−58.
(27) Kleinauskas, A.; Rocha, S.; Sahu, S.; Sun, Y.-P.; Juzenas, P. Carbon-Core Silver-Shell Nanodots as Sensitizers for Phototherapy and Radiotherapy. *Nanotechnology* **2013**, *24*, No. 325103.
(28) Shang, M.; Wang, W.; Sun, S.; Zhou, L.; Zhang, L. Bi_2WO_6 Nanocrystals with High Photocatalytic Activities under Visible Light. *J. Phys. Chem. C* **2008**, *112*, 10407−10411.
(29) Xu, C.; Wei, X.; Ren, Z.; Wang, Y.; Xu, G.; Shen, G.; Han, G. Solvothermal Preparation of Bi_2WO_6 Nanocrystals with Improved Visible Light Photocatalytic Activity. *Mater. Lett.* **2009**, *63*, 2194−2197.
(30) Yang, C.; Huang, Y.; Li, T.; Li, F. Bi_2WO_6 Nanosheets Synthesized by a Hydrothermal Method: Photocatalytic Activity Driven by Visible Light and the Superhydrophobic Property with Water Adhesion. *Eur. J. Inorg. Chem.* **2015**, *2015*, 2560−2564.
(31) Yang, Z.; Huang, L.; Xie, Y.; Lin, Z.; Fan, Y.; Liu, D.; Chen, L.; Zhang, Z.; Wang, X. Controllable Synthesis of Bi_2WO_6 Nanoplate Self-Assembled Hierarchical Erythrocyte Microspheres Via a One-Pot Hydrothermal Reaction with Enhanced Visible Light Photocatalytic Activity. *Appl. Surf. Sci.* **2017**, *403*, 326−334.
(32) Zhang, C.; Zhu, Y. Synthesis of Square Bi_2WO_6 Nanoplates as High-Activity Visible-Light-Driven Photocatalysts. *Chem. Mater.* **2005**, *17*, 3537−3545.
(33) Hu, J.; Chen, D.; Mo, Z.; Li, N.; Xu, Q.; Li, H.; He, J.; Xu, H.; Lu, J. Z-Scheme 2d/2d Heterojunction of Black Phosphorus/Monolayer Bi_2WO_6 Nanosheets with Enhanced Photocatalytic Activities. *Angew. Chem., Int. Ed.* **2019**, *58*, 2073−2077.
(34) Yuan, L.; Weng, B.; Colmenares, J. C.; Sun, Y.; Xu, Y.-J. Multichannel Charge Transfer and Mechanistic Insight in Metal Decorated 2d−2d Bi_2WO_6−TiO_2 Cascade with Enhanced Photocatalytic Performance. *Small* **2017**, *13*, No. 1702253.
(35) Fu, H. B.; Zhang, L. W.; Yao, W. Q.; Zhu, Y. F. Photocatalytic Properties of Nanosized Bi_2WO_6 Catalysts Synthesized Via a Hydrothermal Process. *Appl. Catal., B* **2006**, *66*, 100−110.
(36) Zhang, C.; Ren, J.; Hua, J.; Xia, L.; He, J.; Huo, D.; Hu, Y. Multifunctional Bi_2WO_6 Nanoparticles for CT-Guided Photothermal and Oxygen-Free Photodynamic Therapy. *ACS Appl. Mater. Interfaces* **2018**, *10*, 1132−1146.
(37) Feng, L.; Yang, D.; Gai, S.; He, F.; Yang, G.; Yang, P.; Lin, J. Single Bismuth Tungstate Nanosheets for Simultaneous Chemo-, Photothermal, and Photodynamic Therapies Mediated by Near-Infrared Light. *Chem. Eng. J.* **2018**, *351*, 1147−1158.
(38) Fan, W.; Tang, W.; Lau, J.; Shen, Z.; Xie, J.; Shi, J.; Chen, X. Breaking the Depth Dependence by Nanotechnology-Enhanced X-ray-Excited Deep Cancer Theranostics. *Adv. Mater.* **2019**, *31*, No. 1806381.
(39) Chen, Q.; Wu, J.; Ou, X.; Huang, B.; Almutlaq, J.; Zhumekenov, A. A.; Guan, X.; Han, S.; Liang, L.; Yi, Z.; Li, J.; Xie, X.; Wang, Y.; Li, Y.; Fan, D.; Teh, D. B. L.; All, A. H.; Mohammed, O. F.; Bakr, O. M.; Wu, T.; Bettinelli, M.; Yang, H.; Huang, W.; Liu, X. All-Inorganic Perovskite Nanocrystal Scintillators. *Nature* **2018**, *561*, 88−93.
(40) Gomes, A.; Fernandes, E.; Lima, J. L. F. C. Fluorescence Probes Used for Detection of Reactive Oxygen Species. *J. Biochem. Biophys. Methods* **2005**, *65*, 45−80.
(41) Chen, W.; Ouyang, J.; Yi, X.; Xu, Y.; Niu, C.; Zhang, W.; Wang, L.; Sheng, J.; Deng, L.; Liu, Y.-N.; Guo, S. Black Phosphorus Nanosheets as a Neuroprotective Nanomedicine for Neurodegenerative Disorder Therapy. *Adv. Mater.* **2018**, *30*, No. 1703458.
(42) Yin, W.; Yu, J.; Lv, F.; Yan, L.; Zheng, L. R.; Gu, Z.; Zhao, Y. Functionalized Nano-MoS_2 with Peroxidase Catalytic and Near-Infrared Photothermal Activities for Safe and Synergetic Wound Antibacterial Applications. *ACS Nano* **2016**, *10*, 11000−11011.
(43) Sun, H.; Gao, N.; Dong, K.; Ren, J.; Qu, X. Graphene Quantum Dots-Band-Aids Used for Wound Disinfection. *ACS Nano* **2014**, *8*, 6202−6210.
(44) Lu, K.; He, C.; Guo, N.; Chan, C.; Ni, K.; Lan, G.; Tang, H.; Pelizzari, C.; Fu, Y.-X.; Spiotto, M. T.; Weichselbaum, R. R.; Lin, W. Low-Dose X-Ray Radiotherapy−Radiodynamic Therapy Via Nanoscale Metal−Organic Frameworks Enhances Checkpoint Blockade Immunotherapy. *Nat. Biomed. Eng.* **2018**, *2*, 600−610.
(45) Lei, P.; An, R.; Zhang, P.; Yao, S.; Song, S.; Dong, L.; Xu, X.; Du, K.; Feng, J.; Zhang, H. Ultrafast Synthesis of Ultrasmall Poly(Vinylpyrrolidone)-Protected Bismuth Nanodots as a Multifunctional Theranostic Agent for in Vivo Dual-Modal CT/Photothermal-Imaging-Guided Photothermal Therapy. *Adv. Funct. Mater.* **2017**, *27*, No. 1702018.
(46) Du, Z.; Zhang, X.; Guo, Z.; Xie, J.; Dong, X.; Zhu, S.; Du, J.; Gu, Z.; Zhao, Y. X-Ray-Controlled Generation of Peroxynitrite Based on Nanosized $LiLuF_4$:Ce^{3+} Scintillators and Their Applications for Radiosensitization. *Adv. Mater.* **2018**, *30*, No. 1804046.
(47) Nithya, V. D.; Selvan, R. K.; Kalpana, D.; Vasylechko, L.; Sanjeeviraja, C. Synthesis of Bi_2WO_6 Nanoparticles and Its Electrochemical Properties in Different Electrolytes for Pseudocapacitor Electrodes. *Electrochim. Acta* **2013**, *109*, 720−731.
(48) Nithya, V. D.; Selvan, R. K.; Vasylechko, L.; Sanjeeviraja, C. Effect of Carbon Coating on the Electrochemical Properties of Bi_2WO_6 Nanoparticles by PVP-Assisted Sonochemical Method. *J. Appl. Electrochem.* **2015**, *45*, 473−485.
(49) Nithya, V. D.; Selvan, R. K.; Vasylechko, L.; Sanjeeviraja, C. Surfactant Assisted Sonochemical Synthesis of Bi_2WO_6 Nanoparticles and Their Improved Electrochemical Properties for Use in Pseudocapacitors. *RSC Adv.* **2014**, *4*, 4343−4352.
(50) Li, J.; Lei, N.; Guo, L.; Song, Q.; Liang, Z. Constructing H-BN/Bi_2WO_6 Quantum Dot Hybrid with Fast Charge Separation and Enhanced Photoelectrochemical Performance by Using H-BN for Hole Transfer. *ChemElectroChem* **2018**, *5*, 300−308.
(51) Cui, Y.; Li, H.; Hong, W.; Fan, S.; Zhu, L. The Effect of Carbon Content on the Structure and Photocatalytic Activity of Nano-Bi_2WO_6 Powder. *Powder Technol.* **2013**, *247*, 151−160.
(52) Zhou, Y.; Zhang, Y.; Lin, M.; Long, J.; Zhang, Z.; Lin, H.; Wu, J. C. S.; Wang, X. Monolayered Bi_2WO_6 Nanosheets Mimicking Heterojunction Interface with Open Surfaces for Photocatalysis. *Nat. Commun.* **2015**, *6*, No. 8340.
(53) Nosaka, Y.; Nosaka, A. Y. Generation and Detection of Reactive Oxygen Species in Photocatalysis. *Chem. Rev.* **2017**, *117*, 11302−11336.
(54) He, W.; Kim, H.-K.; Wamer, W. G.; Melka, D.; Callahan, J. H.; Yin, J.-J. Photogenerated Charge Carriers and Reactive Oxygen Species in ZnO/Au Hybrid Nanostructures with Enhanced Photocatalytic and Antibacterial Activity. *J. Am. Chem. Soc.* **2014**, *136*, 750−757.
(55) Rosman, C.; Pierrat, S.; Henkel, A.; Tarantola, M.; Schneider, D.; Sunnick, E.; Janshoff, A.; Sönnichsen, C. A New Approach to Assess Gold Nanoparticle Uptake by Mammalian Cells: Combining Optical Dark-Field and Transmission Electron Microscopy. *Small* **2012**, *8*, 3683−3690.
(56) Klein, N. D.; Hurley, K. R.; Feng, Z. V.; Haynes, C. L. Dark Field Transmission Electron Microscopy as a Tool for Identifying Inorganic Nanoparticles in Biological Matrices. *Anal. Chem.* **2015**, *87*, 4356−4362.

DOI: 10.1021/acsami.9b03636
ACS Appl. Mater. Interfaces XXXX, XXX, XXX−XXX

(57) Mercer, R. R.; Scabilloni, J. F.; Wang, L.; Battelli, L. A.; Antonini, J. M.; Roberts, J. R.; Qian, Y.; Sisler, J. D.; Castranova, V.; Porter, D. W.; Hubbs, A. F. The Fate of Inhaled Nanoparticles: Detection and Measurement by Enhanced Dark-Field Microscopy. *Toxicol. Pathol.* **2018**, *46*, 28−46.
(58) Franken, N. A. P.; Rodermond, H. M.; Stap, J.; Haveman, J.; van Bree, C. Clonogenic Assay of Cells in Vitro. *Nat. Protoc.* **2006**, *1*, 2315−2319.

DOI: 10.1021/acsami.9b03636
ACS Appl. Mater. Interfaces XXXX, XXX, XXX−XXX